Enhancing densification of metakaolin-based geopolymers via the cold sintering process

Abdullah Jabr [a,1], Srečo D. Škapin [b,1,*] , Sara Tominc [c], Nina Daneu [b], Jakob König [b], Vilma Ducman [c], Lidija Korat Bensa [c], Raul Bermejo [a], Matjaž Spreitzer [b]

[a] Department of Materials Science, Montanuniversitaet Leoben, Franz Josef-Strasse 18, A-8700 Leoben, Austria
[b] Advanced Materials Department, "Jožef Stefan" Institute, Jamova cesta 39, 1000 Ljubljana, Slovenia
[c] Slovenian National Building and Civil Engineering Institute, Dimičeva 12, 1000 Ljubljana, Slovenia

A R T I C L E   I N F O

A B S T R A C T

Clay-based materials typically require high-temperature processing (>900 °C), resulting in high energy consumption. This study explores cold sintering of metakaolin (MK) powders to achieve high mechanical strength at significantly lower processing temperatures. By applying uniaxial pressure of 400 MPa and heating to only 240 °C in the presence of 15 mol/L NaOH solution, successful densification of structurally sound and dense samples with an average density of 2.16 g/cm³ and a biaxial flexural strength of ~35 MPa was achieved. This strength surpasses that of conventionally sintered MK (1470 °C) by ~30 %. Densification was found to be governed by synergistic mechanisms involving MK exfoliation, conformal sintering around aggregates, and the precipitation of an amorphous sodium aluminosilicate hydrate phase. Crack formation was avoided through process optimization and verified using X-ray micro-computed tomography. These findings offer new insights into the chemo-mechanical mechanisms of cold sintering and demonstrate its potential as an efficient route for producing structural materials.

1. Introduction

Amid growing concerns about global warming, considerable efforts have been made to improve the sustainability of industrial manufacturing processes. The construction materials manufacturing industry, particularly the cement sector, is highly energy and carbon emission intensive and is the third largest source of CO_2 emissions, accounting for around 8 % of global CO_2 emissions [1,2]. More than 50 % of these emissions come from the thermal decomposition of the raw materials used, such as limestone ($CaCO_3$), which releases CO_2 as a by-product when decomposed into lime (CaO) to produce clinker — the most important reactive component in cement. The combustion of fuels, which is necessary for the heating process to temperatures of well over 1000 °C, is responsible for around 40 % of the emissions produced. The building materials industry is currently taking measures to meet the increasing demands for environmentally friendly and sustainable production. These include transitioning to low-carbon and renewable energy sources, improving process efficiency, carbon capture and

utilization (CCU) and reducing the amount of clinker in cement by replacing it with supplementary cementitious materials (SCM) [2–5]. Recently, geopolymers have emerged as a promising sustainable alternative to cement. They are produced by alkali-activation of aluminosilicate-rich materials. These can be obtained from industrial waste or by-products such as fly ash and blast furnace slag, thus contributing to a circular economy and sustainable waste management. However, sources of such aluminosilicate precursors are becoming increasingly limited due to the decline in the use of coal-fired power plants and the ongoing conversion of steel production away from traditional blast furnace methods [6]. Alternatively, metakaolin has gained interest as a sustainable precursor, since it is derived from the calcination of naturally occurring kaolin clays. This makes it a well-defined material in terms of chemical composition and homogeneity compared to fly ash and slag, ensuring production control in terms of consistency [7,8]. The energy consumption for the calcination of kaolinite clay to produce metakaolin is only 10 % of the energy consumption for cement clinker production, as it usually takes place at

* Corresponding author.
  E-mail address: sreco.skapin@ijs.si (S.D. Škapin).
  [1] Authors contributed equally to this work.

lower temperatures between 600 and 800 °C [8]. Furthermore, there are no carbon emissions during calcination as the by-product is pure water produced during the dehydroxylation of kaolinite, in contrast to the high CO_2 emissions produced during the calcination of limestone in clinker production. As a result, metakaolin has gained considerable importance in recent decades, especially in the field of sustainable production of building materials [7].

The conventional production of metakaolin-based materials is usually based on mold casting processes, which have a relatively high water content. This poses several challenges, including long curing times — often extending over several weeks [9]— increased porosity and an increased risk of cracking [10]. These aspects require careful selection of the paste formulation and curing conditions to minimize cracking, which significantly compromises the structural integrity of the final material [11]. In this study, the cold sintering process (CSP) is proposed as an alternative processing route to enable the rapid production of dense, structurally robust metakaolin-based materials suitable for construction-related applications. CSP is a novel, sustainable sintering process that enables the densification of inorganic materials at temperatures below 300 °C within short periods of time, typically less than one hour [12,13]. The process is based on a chemo-mechanical densification mechanism known as pressure solution creep, which is enabled by an externally applied pressure and a chemically active, transient liquid phase [14]. In general, densification occurs in a serial three-step process of dissolution, diffusion and precipitation driven by chemical potential gradients between particle contacts and pore surfaces. Increased dissolution occurs at highly stressed particle contacts due to the simultaneous action of the applied pressure and chemically active liquid phase [15]. The dissolved species migrate through the liquid phase into areas with low chemical potential (i.e. pores), where precipitation occurs when the liquid phase evaporates, leading to the elimination of the pores. The prerequisites for successful densification in CSP are therefore sufficient solubility of the solid phase in the liquid phase and low stability of the solutes to promote their precipitation. The precipitation step in particular plays a key role in achieving high densification [16].

In this work, a NaOH solution is proposed as a suitable transient liquid phase for the cold sintering process, as it is able to significantly dissolve metakaolin particles [17,18]. Precipitation is expected to occur through the reaction of the dissolved Si and Al species with the Na ions, resulting in the formation of an amorphous sodium aluminosilicate phase commonly referred to as N-A-S-H gel [18,19]. In the context of cold sintering, the formation of this gel is desirable as it has been reported to increase the mechanical (compressive) strength of geopolymers [11,20]. These chemical interactions between metakaolin and NaOH form the basis for effective densification during cold sintering. However, a challenging aspect is the formation of delamination cracks during sintering, which compromise the structural integrity of cold sintered materials. As reported in a previous work, this can be mitigated by controlling the application of pressure and the kinetics of liquid phase evaporation during CSP, resulting in structurally reliable cold sintered ceramics [21].

The aim of this work is to investigate the improved densification and structural integrity of cold sintered metakaolin geopolymers prepared with NaOH solution as a transient liquid phase. The underlying chemical interactions and their effects on densification behaviour and microstructural evolution during CSP are discussed. The elimination of the commonly occurring delamination cracks is demonstrated by an optimised selection of cold sintering parameters and confirmed by destructive mechanical testing and non-destructive X-ray microtomography analyses. The biaxial mechanical strength of CSP geopolymers is evaluated for the first time and compared with conventionally sintered samples of comparable density.

2. Experimental

2.1. Material of study and phase analysis

Commercially available metakaolin (MK), supplied by Argeco Développement, was used for cold and conventional sintering experiments. The measured specific surface area (SSA) of the metakaolin powder is 12.6 m^2/g, determined by single-point nitrogen adsorption, using a Micromeritics FlowSorb II 23,000 instrument. Table 1 shows the chemical composition of the as-received MK, as determined by XRF analysis. The powder primarily consisted of ~26 wt % Al_2O_3 and ~69 wt % SiO_2, along with minor amounts of Fe_2O_3 and TiO_2, which together accounted for 3.45 wt %. Trace oxides including CaO, MgO, Na_2O, K_2O, among others, contributed less than 1.5 wt % collectively. Complementary XRD phase analysis (Fig. 1a) indicated that MK comprises 40.3 wt % quartz, 0.7 wt % anatase and an amorphous phase representing the remaining 59.0 wt %. As can be seen in Fig. 1b, the amorphous phase appears as a broad, low-intensity hump in the 2θ range of 15°–35°, which is typical for various grades of metakaolin powders [11,22,23]. The molar ratio of oxides in the chemical formula of pure MK $(Al_2O_3 \bullet 2SiO_2)$ is $Al_2O_3/SiO_2 = 1:2$, corresponding to a weight ratio of 1:1.18. Based on this ratio, our starting MK can be estimated to contain 58.6 wt % amorphous metakaolin, 40.2 wt % quartz and 1.1 wt % anatase, assuming all other elements besides Al, Si and Ti are incorporated in the MK structure. This estimation agrees well with the Rietveld analysis of the XRD pattern in Fig. 1.

2.2. Sintering of samples

2.2.1. Cold sintering

The powder was prepared for the cold sintering experiments by mixing the MK powder with an aqueous NaOH solution with a concentration of 15 mol/L (Fig. 2). The amount of NaOH solution added varied between 6 and 12 wt %. The starting mixtures were thoroughly homogenised with an agate pestle and mortar for about 5 min. Prolonged homogenization was avoided due to possible water evaporation. The pellets were pressed in a steel die with a diameter of 10 mm. The die was equipped with a heating jacket that allowed heating to a set temperature of 240 °C. The compacts were two-ended uniaxially pressed for 15 min at 400 MPa at RT, followed by a two-stage heating process. According to [24], the dissolution of MK in NaOH reaches its maximum after 10 min of exposure at temperatures between 70 and 100 °C. However, at temperatures above 80 °C, the formation of zeolite precipitates is significantly accelerated, which may consume dissolved ionic species and hinder pressure solution creep. To prevent premature zeolite formation while maximizing MK dissolution, an intermediate step was implemented at 75 °C for 10 min. This step also facilitated the evaporation of excess water. Subsequently, the temperature was increased to the CSP temperature of 240 °C with a dwell time of 15 min, after which the samples were promptly removed from the die. The resulting cold sintered specimens are hereafter referred to as MK-CS.

2.2.2. Conventional sintering

For the conventional sintering experiments, the MK powder was pressed at 150 MPa into discs with a diameter of 10 mm and a height of ~ 3 mm. For each firing temperature, which was varied between 800 °C and 1500 °C with a dwell time of 1 h, five to ten samples were prepared. The heating rate was 5 °C/min. The samples were cooled down with free furnace cooling. These samples are referred to below as "MK" followed by the sintering temperature, e.g. MK1000 refers to the samples sintered at 1000 °C.

2.3. Microstructural characterization techniques

The phase composition of the starting MK and the samples was determined by X-ray powder diffraction (AXS D4 Endeavor, Bruker

Table 1
Composition of metakaolin (in wt %) as determined by XRF.

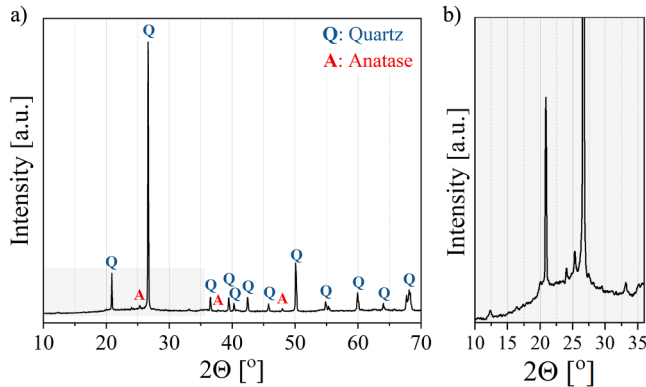| Component	Al_2O_3	SiO_2	CaO	MgO	Fe_2O_3	Na_2O	K_2O	P_2O_5	TiO_2	ZrO_2	BaO	Others
Mass content [wt. %]	25.58	69.46	0.48	0.17	2.32	0.29	0.18	0.06	1.13	0.10	0.04	0.19

Fig. 1. (a) XRD pattern of the as-received metakaolin powder and (b) a close-up of the amorphous broad peak at $2\theta = 15-35$.

Instruments). The morphology of the MK powder and the microstructural characteristics of the densified samples were imaged using a FE-SEM (Thermo Fisher Verios 4 G HP). The microstructures were imaged on fracture surfaces coated with carbon with a thickness of 4–5 nm.

Nanoscale analysis of the cold sintered sample was performed using an aberration-corrected scanning transmission electron microscope (STEM, JEOL ARM-200CF) operated at 200 kV. The microscope was equipped with annular detector for dark-field (DF; 68–180 mrad) and bright-field (BF; 11–22 mrad) imaging and a large solid angle CENTURIO EDX detector for chemical analyses at the nanoscale. The samples for STEM were prepared by cutting, thinning, dimpling and ion-milling with 4 kV Ar ions at an angle of 8 degrees from both sides until perforation. Prior to STEM analyses, the sample was carbon-coated to prevent charging under the electron beam.

Thermogravimetric (TG) characterization and mass spectroscopy (MS) of the MK and densified samples were performed using a thermogravimetric analyzer coupled with a mass spectrometer (TG/DTA/MS; NETZSCH STA 449 C/6/G Jupiter, QMS 403 Aëoloss quadrupole). The evolution of H_2O was monitored by an *m/z* fragment of 18. The heating experiments were conducted in an atmosphere containing 20 % O_2, and 80 % Ar from room temperature to 1200 °C at a heating rate of 10 °C/min.

Chemical composition of the metakaolin (Table 1) was determined by X-ray fluorescence spectroscopy (XRF) using ARL PERFORM'X

(Thermo Fisher Scientific INC., Ecublens, Switzerland) and the Uni-Quant 5 software (Thermo Fisher Scientific Inc., Waltham, MA, USA).

The theoretical density of metakaolin was determined as 2.6 g/cm^3 using Helium pycnometry (AccuPyc II 1340, Micromeritics). The sintering curve of conventionally sintered MK was recorded by using a heating microscope (Hesse Instruments), which operated up to 1450 °C.

Solubility tests of MK in 15 mol/L NaOH were carried out at room temperature and at 75 °C in a Teflon beaker. A total of 0.5 g powder was dispersed in 10 mL NaOH and mixed with a magnetic stirrer for 40 min. This time corresponded to the time for cold sintering where MK was in contact with NaOH, considering an estimated boiling point of the hydroxide solution of ~125 °C. The dispersions were then centrifuged at 10,000 rpm for 9 min. The resulting supernatants were analyzed by inductively coupled plasma (ICP) analysis using ICP-OES Varian 715-ES with Sample Preparation System SP 3.

X-ray micro-computed tomography (micro-CT) was employed for the non-destructive characterization of defects in cold sintered pellets using microXCT400 tomograph (XRadia, Concord, CA, USA). Data for each sample were collected with a macro lens (0.39 × magnification) at 80 keV acceleration voltage. Each projection image was acquired using a 1 s exposure time and a 22 μm pixel size; 1600 images were captured in total. Following 3D tomographic image reconstruction, a commercial software program AVIZO Fire *(Thermo Fisher Scientific)* was used for visualizing the internal sample structure.

2.4. Strength measurements and evaluation

The mechanical strength of the prepared samples was tested using the ball-on-three-balls (B3B) test. In this test, biaxial bending is induced in disc-shaped specimens by applying a central load with one ball while the specimen is supported by three balls on the opposite side. In this work, balls with a diameter of 7.14 mm were used to test specimens with a diameter of 10 mm. All tests were performed using a universal testing machine (Zwick Z010, Zwick GmbH & Co. KG, Ulm, Germany) at a loading rate of 0.5 mm/min. The bending strength was calculated from the maximum stress at fracture as follows [25]:

$$\sigma_{max} = f \cdot \frac{F}{t^2} \qquad (1)$$

where *F* is the fracture load, *t* is the thickness of the specimen and *f* is a dimensionless factor that depends on the Poisson's ratio and the loading configuration (specimens and ball geometry). The Poisson's ratio for MK
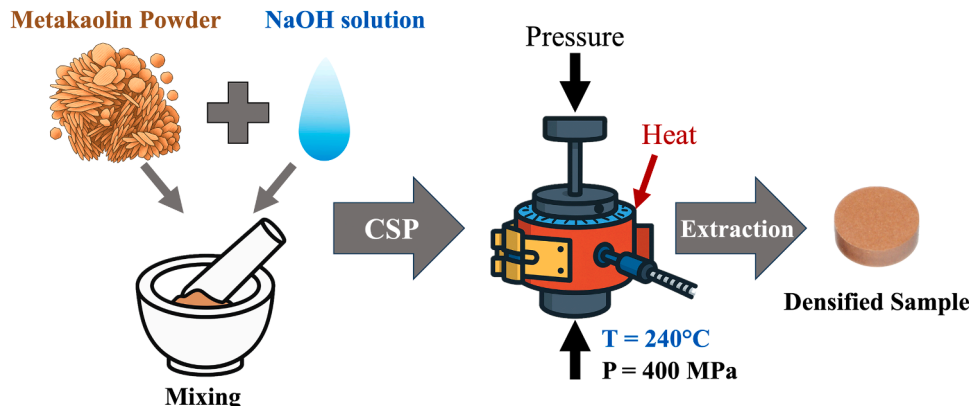

Fig. 2. Schematic representation of cold sintering process to densify MK.

was assumed to be 0.25 as reported in [26]. At least three specimens per sample set were tested to evaluate the average strength.

3. Results and discussion

3.1. Cold sintering densification and microstructure

Fig. 3a shows the morphology of the starting powder, which consists of large agglomerates up to 15 μm in size. These agglomerates are loosely bound and can be crushed and homogenized with an agate mortar and pestle, similar to the treatment in the CSP experiments (Fig. 3b). Large quartz particles (~5 μm) are embedded in MK particles in the submicron range, as shown in Fig. 3b The MK particles exhibit a hexagonal platelet-like morphology with an average size of about 200 nm (Fig. 3c).

Cold sintering of MK resulted in samples with an average density of 2.16 g/cm^3, which is slightly higher than the values reported in previous studies on densification of metakaolin-based geopolymers using different techniques, including conventional curing [27], high-pressure densification [28] and hot pressing [27]. Furthermore, this result is in good agreement with a recent study on cold sintering of MK using an alkaline solution of sodium silicate as a transient liquid phase [23]. As can be seen in Fig. 3, compaction of the powder requires densification of the MK platelets around the embedded quartz particles, resulting in a composite material. Fig. 4 shows the microstructure of cold-sintered MK and illustrates the strong cohesion of the MK matrix with the quartz inclusions. As can be seen in Fig. 4a, the transgranular fracture of the relatively small quartz particles (< 5 μm) indicates strong interfacial bonding and low interfacial porosity. Multiple densification mechanisms have been reported in the cold sintering of composite materials, including enhanced particle rearrangement in flake-like fillers by shearing along inclusions/grains [29,30], or grain boundary sliding and pressure solution creep, as demonstrated in systems such as hexagonal boron nitride flakes combined with sodium molybdate [31]. In the present study, the densification of MK containing quartz inclusions can be attributed to a combination of mechanisms: enhanced rearrangement of MK platelets—facilitated by their layered atomic structure—and pressure solution creep, which promotes densification along the surfaces of quartz particles. This leads to improved interfacial conformity and bonding of the MK matrix around the quartz inclusions. Such conformal sintering was reduced along large quartz particles (~10 μm) due to hindered interfacial accommodation. This resulted in interfacial porosity, which can affect the bond strength at the interface, as shown by the interfacial fracture along large quartz particles (Fig. 4b). It has been reported that densification of such a composite system by conventional sintering methods is either hindered or structurally compromised by the formation of cracks due to constraint sintering effects. Constrained sintering is a major limiting factor in the densification of composites consisting of a matrix that densifies around non-densifying inclusions. This issue arises due to internal (tensile) stresses in the matrix that develop with progressive densification shrinkage [32,33]. However, this phenomenon has not been observed in this work, owing to the low temperatures of CSP and its pressure solution creep mechanism, allowing densification to occur along "constraining" interfaces. A similar observation was reported in a previous work on cold sintering of a matrix of BaTiO$_3$ nanoparticles around microsized BaTiO$_3$ grains [34]. Similarly, the role of interfacial bonding strength has been reported in a previous work on room temperature fabrication of SrTiO$_3$-based composites [35].

The densification of the MK matrix showed a certain degree of heterogeneity related to the alignment of the platelets with respect to the direction of the applied pressure. Enhanced densification was observed in regions where the MK platelets were well aligned (Fig. 5a). As can be seen in Fig. 5b, regions with randomly oriented platelets showed limited densification due to poor platelet packing and reduced particle-particle contacts. The deviation from an ideal homogeneous microstructure was expected due to the random orientation of the platelets at the beginning of the process, which aligned under the effect of uniaxial pressure. In addition, an inhomogeneous distribution of the liquid phase and differences in the compressibility of quartz particles and MK platelets could also contribute to the heterogeneity of the microstructure. Fig. 5c shows the microstructure on the surface perpendicular to the direction of the applied pressure. As can be seen, the bound MK particles show rounded edges, indicating effective dissolution by the NaOH solution in the CSP. This proves the effectiveness of the NaOH solution as a transient liquid phase in the cold sintering of MK, which follows a similar mechanism as observed in geopolymerization [36].

The cold sintering literature widely recognizes that favorable liquid phases for low-temperature densification are those with high dissolution capability while simultaneously forming metastable intermediate species that enable reprecipitation during the final stage of CSP [14,16]. To understand the densification mechanism of MK, dissolution tests of MK in NaOH were performed. At room temperature, the dissolved Al content was 771 ppm, compared to 567 ppm for Si. The dissolution was significantly increased at 75 °C, which represents the intermediate heating step in CSP. At this temperature, Si was dissolved more than Al, with concentrations of 4542 ppm and 4505 ppm, respectively. The values are slightly higher than those reported by Granizo et al. [18], which can be attributed to the higher alkalinity used in this study, i.e. 15 mol/L vs. 8 mol/L. This indicates that the dissolution of MK in NaOH starts incongruently and converges to congruence with accelerated and/or progressive kinetics, i.e. with increasing time and temperature. This observation was also reported by Chen et al. [17]. Incongruent dissolution is one of the limiting factors for achieving high densification in CSP, as the preferential dissolution of one of the ions leads to surface passivation of the particles, which separates the liquid from the solid phase. However, this mechanism did not limit the densification of MK under the CSP conditions used, which is due to the transient incongruent dissolution. The preferential leaching of Al during dissolution of MK in alkaline solution is attributed to the weaker Al–O bonds compared to Si–O bonds, which are more easily nucleophilically attacked by the OH ions of the hydroxide in the early stages of dissolution. However, this slows down as dissolution progresses and the solution becomes saturated with Al, allowing for congruency to be reached [17]. To
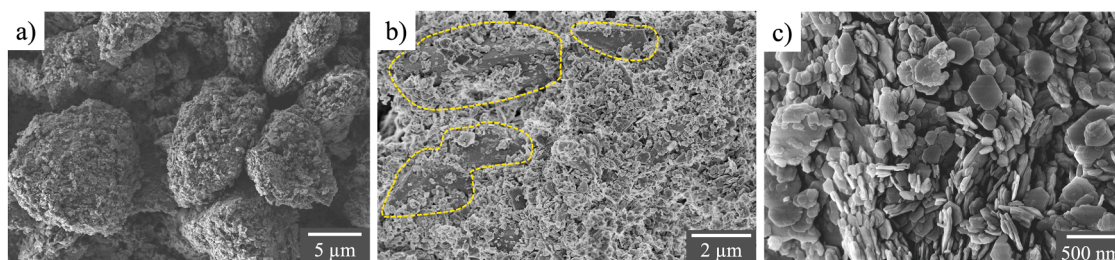

Fig. 3. Representative SEM micrographs of commercial MK: a) as-received, b) treated in agate mortar and pestle for 5 min, containing larger quartz particles (highlighted by yellow dashed lines), c) micrograph taken at larger magnification showing hexagonal MK platelet particles.
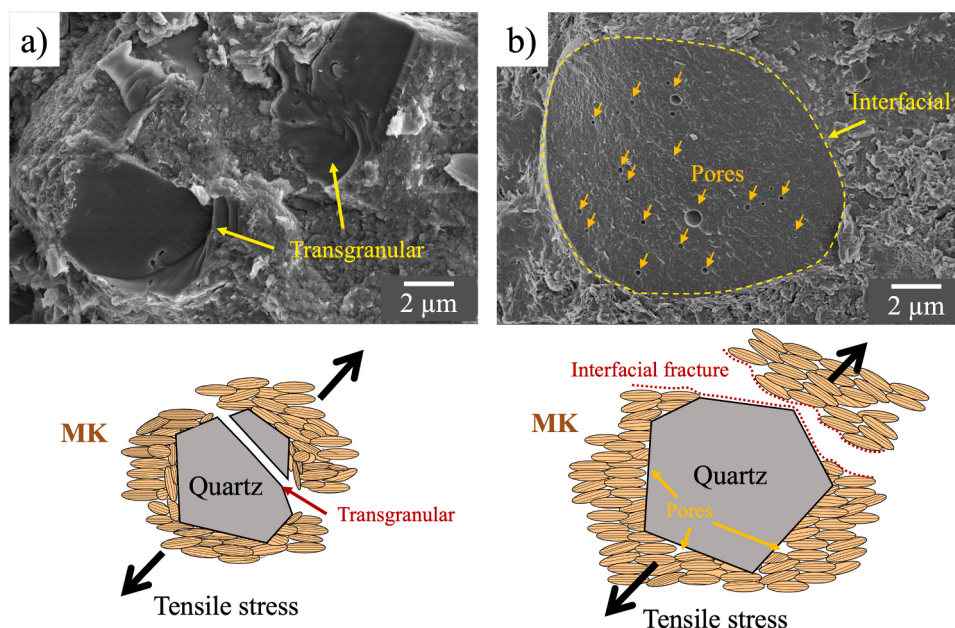
Fig. 4. Representative microstructure images of fractured surfaces of MK-CS show embedded quartz grains in the MK matrix: (a) transgranular fracture of small quartz grains (< 5 μm) due to their strong bonding to MK, and (b) interfacial separation of a large quartz grain (~ 10 μm) due to interfacial porosity arising from reduced conformation along large quartz surfaces.

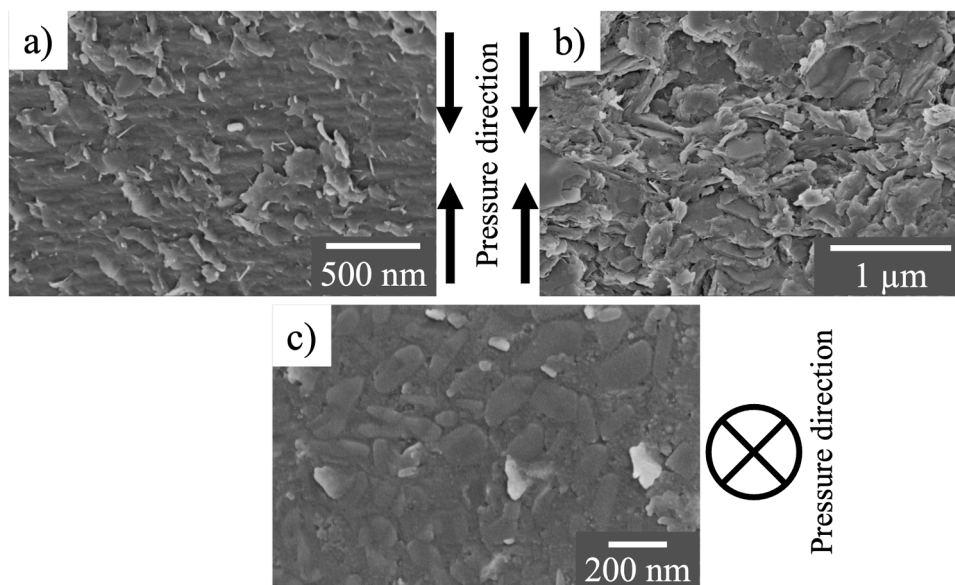**Fig. 5.** Representative SEM micrographs of the MK matrix in MK-CS: a) well-aligned platelets result in high densification and b) densification is affected by the random orientation of the platelets. The cross-section plane with respect to the direction of applied pressure is parallel in (a) and (b) and normal in (c).

understand the densification mechanism, TEM analysis was performed.

Fig. 6 shows TEM imaging of cold-sintered MK. It confirms that the sample consists of quartz grains embedded in an amorphous metakaolin matrix. Most of the contacts between the quartz grains and the matrix indicate a close bond between the two phases (Fig. 6a). As can be seen in Fig. 6b, a closer examination of the metakaolin matrix shows that it is composed of exfoliated lamellae with diameters ranging from a few tens of nanometers down to a few nanometers. The actual thickness of the lamellae could be even smaller, as the lamellae are usually not in perfect edge-on orientation. The exfoliation of MK is caused by its dissolution during exposure to NaOH solution. This phenomenon has been documented by numerous researchers who have studied the dissolution of MK in alkaline solutions [19,37]. MK exfoliation positively affects CSP

densification by enhancing particle rearrangement through the shearing of exfoliated flakes into unfilled voids and along inclusions under applied pressure, similar to the behavior observed in systems containing hexagonal boron nitride flakes [29,30]. Additionally, exfoliation promotes congruent dissolution by increasing the reactive surface area accessible to the alkaline solution. Chen et al. reported that the incongruent dissolution of MK in NaOH is transient and that congruent dissolution is enhanced at higher NaOH concentrations [17]. They attributed the enhanced congruent dissolution at higher alkalinity to the exfoliation of MK during dissolution, which exposes the interior of the particles to the alkaline solution. Exfoliation causes the dissolution process not to be limited by the "leaching" of ions from the surface, thereby promoting congruency. The dissolved Al and Si ion complexes
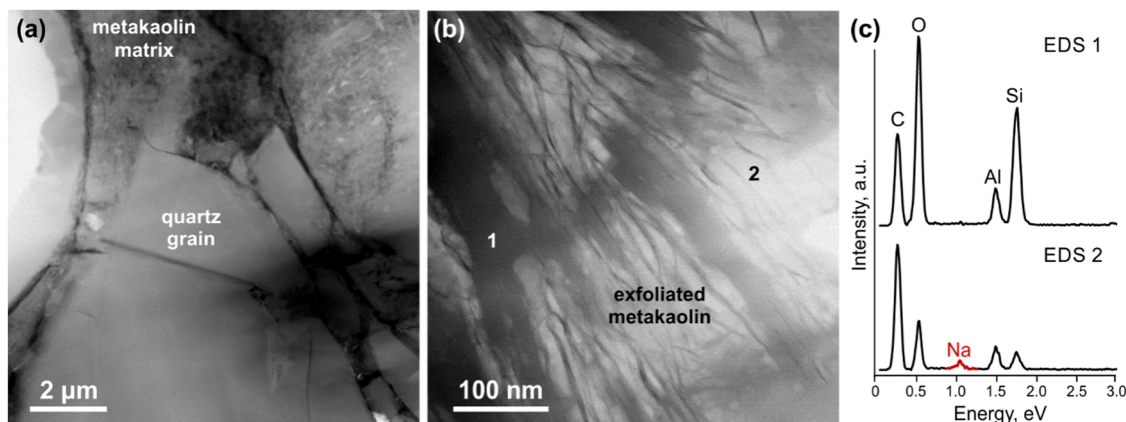
Fig. 6. (a) STEM image showing tight bonding between the quartz particles embedded in the metakaolin matrix. The cracks formed during mechanical TEM specimen preparation and preferential ion milling. (b) Enlarged image of the metakaolin matrix showing its exfoliated texture. The darker layers (1) belong to the original metakaolin, while the brighter regions (2) were formed during the dissolution and exfoliation of the metakaolin under the influence of the NaOH solution. (c) EDS analysis of the darker regions shows only the presence of Si and Al, while the brighter regions contain Na and relatively more Al (less Si) compared to the original metakaolin, indicating preferential dissolution of Al from metakaolin. The EDS results are qualitative due to the low count rate (thin sample and short acquisition time due to rapid sample damage and contamination) and the lack of standards.

diffuse through the liquid phase and precipitate, forming an amorphous sodium aluminosilicate hydrate phase, also known as N-A-S-H gel [11, 18]. This is evidenced by the EDS analysis of the newly formed phase in Fig. 5c, which shows the incorporation of Na into its structure. This amorphous gel phase acts as a bonding phase between the metakaolin particles and provides the mechanical strength to the material, as reported by Duxson et al. [11,20]. It is important to emphasize that the observed cold sintering mechanisms are strongly influenced by the chemical composition of the MK used. The MK in this work can be regarded as silica-rich, which promotes extensive dissolution and facilitates densification with NaOH alone.

The XRD analysis of MK-CS shows the same phase composition as that of the MK starting powder (Fig. 7), consisting of quartz, anatase and an amorphous phase. The Rietveld analysis revealed an increased amount of an amorphous phase, which supports the TEM observation of the newly formed N-A-S-H gel during CSP. The amorphous phase content increased from 59 wt % to a final value of about 75 %, while the quartz content decreased from ~40 wt % to about 24 wt %. In addition, the content of anatase decreased slightly from 0.7 wt % to 0.3 wt %.

The thermogravimetric analysis also indicates the formation of an amorphous phase by cold sintering (Fig. 8). Fig. 8a shows the corresponding TGA curves of the as-received MK powder and the corresponding cold sintered sample MK-CS. A total mass loss of 2 wt % in the

starting powder is due to the loss of physically adsorbed water and the complete dehydroxylation of residual kaolinite. For MK-CS, a higher total mass loss of ~5 wt % was observed, which can be attributed to the decomposition of the newly formed amorphous phase in CSP in addition to the physically adsorbed water. Fig. 8b shows the MS analysis to illustrate the temperatures at which water is released. It shows that for both samples the mass loss up to ~200 °C is due to the loss of physically adsorbed water and nanoscale trapped interlayer water [38]. The dehydroxylation of residual kaolinite in the MK powder can be recognized by the shallow peak extending between 450 °C and 700 °C, which is consistent with previous studies on the dehydroxylation temperature of kaolinite [8,39]. The mass loss between 200 °C and 450 °C was previously described as a consequence of dehydration due to the reorganization of the octahedral layered structure of kaolinite [8]. For cold sintered MK, the MS shows a peak between 300 °C and 400 °C, which is due to the release of hydrate water from the amorphous sodium aluminosilicate hydrate, forming a hydroxo-sodalite phase [40].

The structural integrity of cold-sintered MK showed a strong dependence on the content of water added to the powder, i.e. the amount of liquid phase. The densification of MK showed no correlation with the liquid phase content, as it was almost constant at around 2.16 g/cm³ with a liquid phase content between 6 and 12 wt %. This indicates that the NaOH concentration of 15 mol/L was effective in densifying MK even at low liquid phase contents. However, the structural integrity was significantly affected by low liquid phase content, as shown by the non-destructive micro-CT analysis in Fig. 9. As can be seen in Fig. 9a, a low liquid phase content of 6 wt % resulted in a densified sample, but with multiple delamination cracks. This was alleviated by increasing the liquid phase content to 12 wt. %, resulting in homogenously densified crack-free samples (Fig. 9b). The nature of the delamination cracks (horizontally oriented) in Fig. 9a suggests that the cracking is due to a pressure effect caused by reduced rearrangement of the particles, which is facilitated in CSP by the wetting of the particles by the liquid phase. When the liquid phase content is low, incomplete wetting of the particles leads to limited rearrangement of the particles and poor alignment of the platelet with respect to the applied pressure. This observation of the role of water and its content on the structural integrity of cold-sintered MK is confirmed by boiling tests in a recent study, which showed complete disintegration of cold-sintered samples with low moisture content in contrast to those cold sintered with higher moisture content [23].
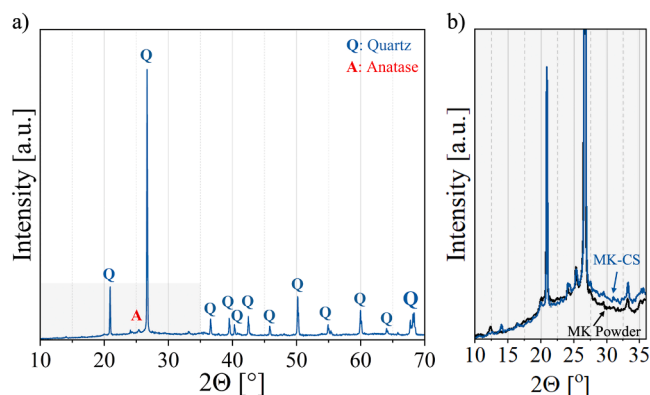

Fig. 7. (a) XRD pattern of cold sintered MK (MK-CS) with diffraction peaks labelled "Q" and "A" corresponding to quartz and anatase, respectively; (b) magnified view of the broad amorphous hump in the 2θ range of 15–35°, with the amorphous peak of the starting powder included for comparison.
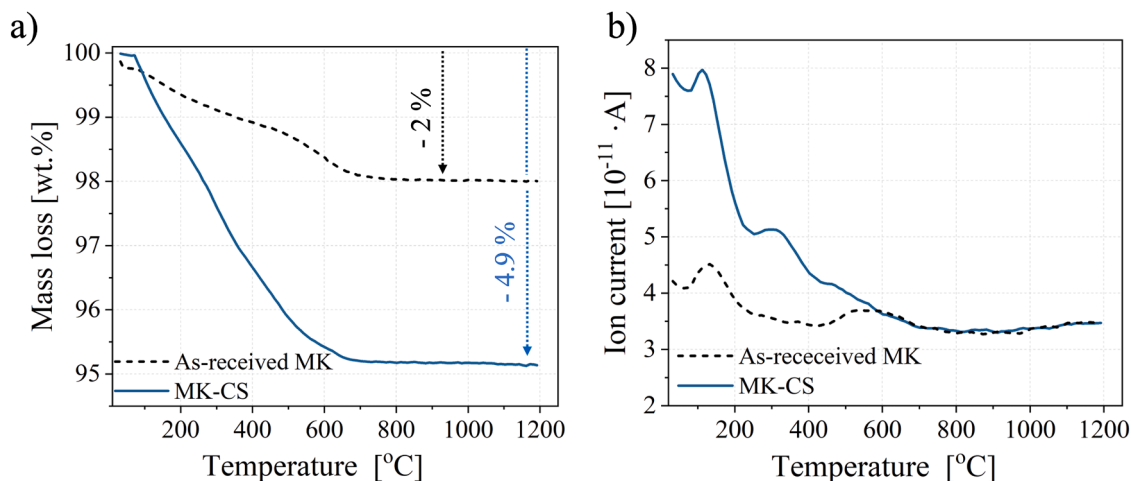
Fig. 8. TGA analysis of the starting MK powder and cold sintered samples (MK-CS): a) mass loss over temperature and b) mass spectrometry of water ($m/z = 18$).
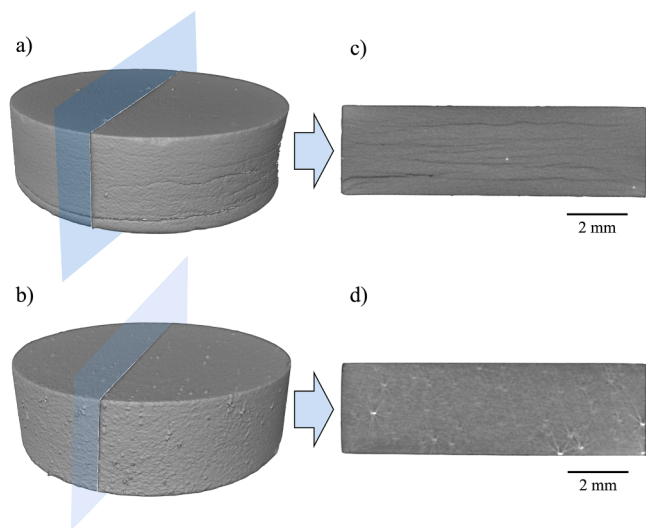

Fig. 9. Micro-CT 3D images of cold sintered MK using 15 mol/L NaOH solution with an amount of: a) 6 wt % and b) 12 wt %. The corresponding cross-sectional views are depicted in c) and d), respectively.

3.2. Densification during conventional sintering

To verify the densification and structural integrity of MK-CS, conventional high-temperature sintering of MK was also performed. Conventional curing techniques were intentionally avoided as they result in MK with lower density, which limits the validity of a direct comparison with MK-CS. High-temperature sintering has been reported to eliminate porosity in MK by forming spinel-like phases which nucleate as nanoscale structures and effectively reduce porosity [38,41].

Fig. 10 shows the sintering curve of the MK powder compact during heating to 1450 °C together with the phase evolution at high temperatures detected by XRD. The expansion of ~1 % up to a temperature of ~450 °C could be attributed to thermal expansion, which is compensated at higher temperatures by the shrinkage associated with the dehydroxylation process [38]. Significant shrinkage begins at ~900 °C, which can be attributed to the onset of densification of the short-range ordered MK. The XRD pattern (Fig. 10b) reveals no newly formed phases at this temperature. At 1000 °C, a small amount of the mullite phase begins to form, as can be seen from the XRD pattern in Fig. 10b Previous studies reported that the onset of formation of nanosized mullite and/or spinel-type phases occurs at ~980 °C [41,42]. The formation of spinel at

this temperature cannot be excluded in this work, as its nanoscale crystalline form is below the detection limit of XRD and its amorphous form is transparent to X-rays. The onset of the second shrinkage step at ~1100 °C coincides with the growth of mullite. Crystallization of amorphous, silica-rich phases to cristobalite was been demonstrated in samples sintered at 1200 °C, which is in good agreement with previous studies reporting the evolution of cristobalite at temperatures ≥1200 °C [38]. At higher temperatures, the formation of cristobalite and mullite increases at the expense of quartz. These results seem to agree with other studies reporting the formation of mullite by the reaction of spinel phases with excess SiO_2 at 1275 °C and the crystallization of secondary mullite at 1300 °C [41,42]. The broad cristobalite reflections suggest that the cristobalite phase forms in nanosized or poorly crystallized grains. At 1500 °C, the quartz is almost completely consumed and forms mullite and cristobalite. The increasing shrinkage at temperatures above 1200 °C can be attributed to the densification and growth of the increasingly developing crystalline phases in the multiphase samples. This is confirmed by the increasing density with increasing temperature, as shown in Table 2. A comparison of the relative density values of cold sintered and high temperature sintered MK samples shows that cold sintering leads to a relative density of ~83 %, which can be achieved conventionally at high temperatures above 1470 °C.

3.3. Mechanical strength results

The evolution of the mechanical strength and the relative density as a function of the sintering temperature for MK-CS and conventionally sintered MK is shown in Fig. 11 and summarized in Table 3. Fig. 11a shows the biaxial bending strength of MK samples sintered at different temperatures. The strength of conventionally sintered MK increases with increasing sintering temperature and ranges from ~10 MPa for MK1350 to ~60 MPa for MK1500. This increase correlates with an increase in relative density from 67 % to 85 % as the sintering temperature increases from 1350 °C to 1500 °C (Fig. 11b). It is noteworthy that the strength of MK-CS is about 35 MPa, exceeding the strength of MK1470, although it was achieved at a sintering temperature of 240 °C. This high strength of MK-CS is due to the high strength of the amorphous N-A-S-H gel formed between the MK particles during cold sintering and its strong interfacial bonding with the embedded quartz particles, as explained in Section 3.1. The high mechanical strength of this amorphous phase in geopolymers has already been emphasized by Duxson et al. under compressive loading [11]. Fig. 11c shows the fracture pattern of a representative set of samples. The fracture of all samples initiated in the center, where the maximum biaxial tensile stress is generated in the B3B test. Most samples fractured into two pieces; however, MK-CSP and
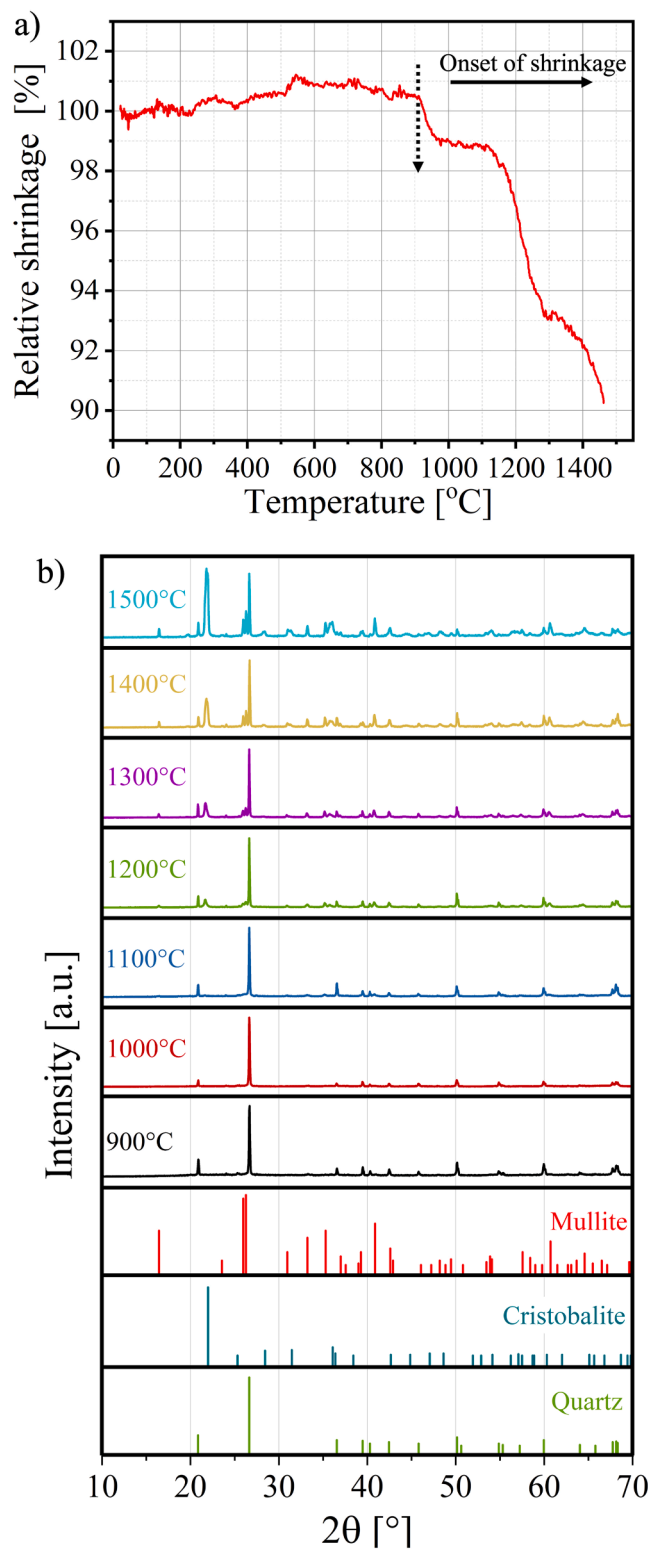
Table 2

Average geometrical density of conventionally sintered MK at different temperatures for 1 h.

Sintering Temperature [°C]	1300	1350	1400	1450	1470	1500
Density [g/cm³]	1.72 ± 0.01	1.73 ± 0.02	1.74 ± 0.02	1.80 ± 0.02	2.02 ± 0.06	2.21 ± 0.03

MK1470 specimens occasionally fractured into three pieces. The almost 80 % higher strength of MK1500 compared to MK-CS could be attributed to three possible reasons: (i) the slightly higher relative density of MK1500, (ii) the higher strength of the grain boundaries between the crystalline phases compared to that of the amorphous N-A-S-H gel in MK-CS, and (iii) the role of quartz particles embedded in an amorphous MK matrix in MK-CS acting as stress concentration sites. These are thermally decomposed in MK1500, resulting in an almost diphasic crystalline material composed of mullite and cristobalite. The role of quartz particles in mechanical failure is supported by the more than twofold increase in strength after sintering at 1500 °C due to their decomposition and the formation of crystalline sintered phases (~27 MPa for MK1470 vs. ~60 MPa for MK1500).

Despite the promising results, this study has certain limitations that merit further investigation. Future research should evaluate the long-term durability and environmental resistance of the cold-sintered MK geopolymers to confirm suitability for real-world structural applications. While a high NaOH concentration facilitated effective dissolution, its potential impact on efflorescence or environmental leaching has not been assessed. Moreover, the current work was limited to uniaxial pressing under high pressures at laboratory-scale dimensions. To translate CSP into industrial practice, future research should explore process scalability and the integration of supplementary materials or additives to reduce pressure requirements and tailor performance.

4. Conclusions

This study demonstrates that CSP is a viable alternative for the rapid low-temperature consolidation of metakaolin-based materials. The resulting densified materials exhibit higher density and mechanical strength than those produced by conventional processing methods. Although the powder consisted of platelet-shaped MK particles and various inclusions such as quartz particles and titanium oxide, densification was not hindered due to the high reactivity of the amorphous MK phase under CSP conditions. Successful densification was found to depend on two key factors: the efficient packing of the platelet-like particles under the applied pressure and the congruent dissolution of MK. The former was improved by increasing the liquid content, which facilitated the rearrangement of the particles along the direction of the applied pressure, resulting in structurally sound, cold-sintered MK, as confirmed by non-destructive micro-CT analysis. The latter was effectively activated by a highly concentrated NaOH solution (15 mol/L), which promoted congruent dissolution by exfoliation of the MK particles, as shown by solubility tests and TEM analysis. The mechanism of pressure solution creep densification enabled conformal sintering of the MK matrix around the quartz inclusions, eliminating interfacial porosity and increasing strength. The precipitation of the dissolved species was found to occur through the formation of an amorphous sodium aluminosilicate hydrate phase, which is responsible for the high strength of the material. Although the embedded quartz particles may act as stress concentration sites, cold sintered MK exhibited ~30 % higher biaxial bending strength than conventionally sintered MK at 1470 °C, highlighting improved interfacial bonding through conformal sintering in CSP.
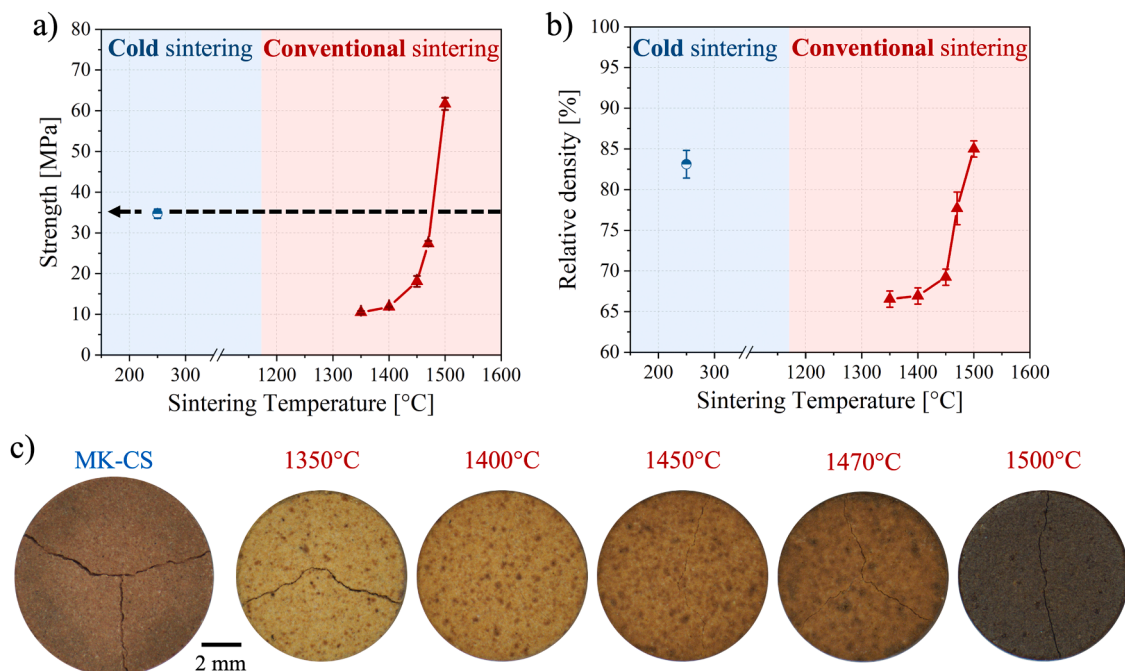
Fig. 10. a) Linear shrinkage of green MK pellet as a function of temperature during sintering in the heating step. b) XRD patterns of MK samples sintered at temperatures ranging from 900 °C to 1500 °C. Reference patterns for quartz (PDF#46–1045), cristobalite (PDF#39–1425), and mullite (PDF#15–0776) were obtained from the ICDD database.

Fig. 11. Comparison between cold-sintered and conventionally sintered MK, showing the effect of sintering temperature on: (a) biaxial strength, (b) relative density and (c) physical appearance and fracture paths of representative samples. The scale bar in (c) is valid for all samples.

Table 3
Average biaxial bending strength and average relative density of cold and conventionally sintered MK, along with their standard deviation.

Sample	Average Strength [MPa]	Average relative density [%]
MK-CS	34.7 ± 1.1	83.1 ± 1.7
MK1350	10.5 ± 0.4	66.5 ± 0.01
MK1400	11.8 ± 0.1	66.9 ± 0.01
MK1450	18.1 ± 1.3	69.2 ± 0.01
MK1470	27.4 ± 1.6	77.7 ± 0.02
MK1500	61.7 ± 1.5	85.0 ± 0.01

Author contributions

Abdullah Jabr: Writing–original draft, Methodology, Investigation, Formal analysis, Visualization. **Srečo D. Škapin:** Writing-original draft, Methodology, Investigation, Formal analysis, Conceptualization, Supervision, Funding acquisition. **Sara Tominc:** Investigation. **Nina Daneu:** Investigation. **Jakob König:** Writing-Review&Editing, Funding acquisition. **Vilma Ducman:** Writing-Review&Editing, Funding acquisition. **Lidija Korat:** Methodology. **Raul Bermejo:** Writing-Review&Editing, Supervision. **Matjaž Spreitzer:** Supervision, Funding acquisition.

CRediT authorship contribution statement

Abdullah Jabr: Writing – original draft, Visualization, Methodology, Investigation, Formal analysis. **Srečo D. Škapin:** Writing – original draft, Supervision, Methodology, Investigation, Funding acquisition, Formal analysis, Conceptualization. **Sara Tominc:** Investigation. **Nina Daneu:** Investigation. **Jakob König:** Writing – review & editing, Funding acquisition. **Vilma Ducman:** Writing – review & editing, Funding acquisition. **Lidija Korat Bensa:** Methodology. **Raul Bermejo:** Writing – review & editing. **Matjaž Spreitzer:** Supervision, Funding acquisition.

Declaration of competing interest

The authors declare that they have no known competing financial interests or personal relationships that could have appeared to influence the work reported in this paper.

Acknowledgments

References

[1] R.M. Andrew, Global CO_2 emissions from cement production, Earth Syst. Sci. Data 10 (2018) 195–217, https://doi.org/10.5194/essd-10-195-2018.

[2] D. Cheng, D.M. Reiner, F. Yang, C. Cui, J. Meng, Y. Shan, Y. Liu, S. Tao, D. Guan, Projecting future carbon emissions from cement production in developing countries, Nat. Commun. 14 (2023) 8213, https://doi.org/10.1038/s41467-023-43660-x.

[3] J. Farfan, M. Fasihi, C. Breyer, Trends in the global cement industry and opportunities for long-term sustainable CCU potential for power-to-X, J. Cleaner Prod. 217 (2019) 821–835, https://doi.org/10.1016/j.jclepro.2019.01.226.

[4] P.S. Fennell, S.J. Davis, A. Mohammed, Decarbonizing cement production, Joule Comment. 5 (2021) 1305–1311, https://doi.org/10.1016/j.joule.2021.04.011.

[5] M.C.G. Juenger, R. Snellings, S.A. Bernal, Supplementary cementitious materials: new sources, characterization, and performance insights, Cem. Concr. Res. 122 (2019) 257–273, https://doi.org/10.1016/j.cemconres.2019.05.008.

[6] R. Snellings, P. Suraneni, J. Skibsted, Future and emerging supplementary cementitious materials, Cem. Concr. Res. 171 (2023) 107199, https://doi.org/10.1016/j.cemconres.2023.107199.

[7] Z. Zhang, Y.C. Wong, A. Arulrajah, S. Horpibulsuk, A review of studies on bricks using alternative materials and approaches, Constr. Build. Mater. 188 (2018) 1101–1118, https://doi.org/10.1016/j.conbuildmat.2018.08.152.

[8] B. Ilic, A. Mitrovic, L. Milicic, Thermal treatment of kaolin clay to obtain metakaolin, Hem. Ind. 64 (2010) 351–356, https://doi.org/10.2298/HEMIND100322014I.

[9] N. Ranjbar, C. Kuenzel, J. Spangenberg, M. Mehrali, Hardening evolution of geopolymers from setting to equilibrium: a review, Cem. Concr. Compos. 114 (2020) 103729, https://doi.org/10.1016/j.cemconcomp.2020.103729.

[10] I.P. Segura, P.A. Jensen, A.J. Damø, N. Ranjbar, L.S. Jensen, M. Canut, Influence of sodium-based activators and water content on the fresh and hardened properties of metakaolin geopolymers, SN Appl. Sci. 4 (2022) 283, https://doi.org/10.1007/s42452-022-05167-w.

[11] P. Duxson, A. Fernández-Jiménez, J.L. Provis, G.C. Lukey, A. Palomo, J.S.J. Van Deventer, Geopolymer technology: the current state of the art, J. Mater. Sci. 42 (2007) 2917–2933, https://doi.org/10.1007/s10853-006-0637-z.

[12] A. Ndayishimiye, M.Y. Sengul, T. Sada, S. Dursun, S.H. Bang, Z.A. Grady, K. Tsuji, S. Funahashi, A.C.T. van Duin, C.A. Randall, Roadmap for densification in cold sintering: chemical pathways, Open Ceramics 2 (2020) 100019, https://doi.org/10.1016/j.oceram.2020.100019.

[13] J.-P. Maria, X. Kang, R.D. Floyd, E.C. Dickey, H. Guo, J. Guo, A. Baker, S. Funihashi, C.A. Randall, Cold sintering: current status and prospects, J. Mater. Res. 32 (2017) 3205–3218, https://doi.org/10.1557/jmr.2017.262.

[14] A. Ndayishimiye, S.H. Bang, Christopher.J. Spiers, C.A. Randall, Reassessing cold sintering in the framework of pressure solution theory, J. Eur. Ceram. Soc. (2023) 1–13, https://doi.org/10.1016/j.jeurceramsoc.2022.09.053.

[15] E.H. Rutter, Pressure solution in nature, theory and experiment, J . Geol. Soc. London 140 (1983) 725–740, https://doi.org/10.1144/gsjgs.140.5.0725.

[16] A. Jabr, J. Fanghanel, Z. Fan, R. Bermejo, C. Randall, The effect of liquid phase chemistry on the densification and strength of cold sintered ZnO, J. Eur. Ceram. Soc. 43 (2023) 1531–1541, https://doi.org/10.1016/j.jeurceramsoc.2022.11.071.

[17] X. Chen, B. Jin, P. Suraneni, Understanding the dissolution of metakaolin in sodium hydroxide solutions, Mater. Struct. 57 (2024) 102, https://doi.org/10.1617/s11527-024-02365-3.

[18] N. Granizo, A. Palomo, A. Fernandez-Jiménez, Effect of temperature and alkaline concentration on metakaolin leaching kinetics, Ceram. Int. 40 (2014) 8975–8985, https://doi.org/10.1016/j.ceramint.2014.02.071.

[19] C.E. White, J.L. Provis, A. Llobet, T. Proffen, J.S.J. Van Deventer, Evolution of local structure in geopolymer gels: an In situ neutron pair distribution function analysis, J. Am. Ceram. Soc. 94 (2011) 3532–3539, https://doi.org/10.1111/j.1551-2916.2011.04515.x.

[20] P. Duxson, J.L. Provis, G.C. Lukey, S.W. Mallicoat, W.M. Kriven, J.S.J. Van Deventer, Understanding the relationship between geopolymer composition, microstructure and mechanical properties, Colloids Surf., A 269 (2005) 47–58, https://doi.org/10.1016/j.colsurfa.2005.06.060.

[21] A. Jabr, H.N. Jones, A.P. Argüelles, S. Trolier-McKinstry, C. Randall, R. Bermejo, Scaling up the cold sintering process of ceramics, J. Eur. Ceram. Soc. 43 (2023) 5319–5329, https://doi.org/10.1016/j.jeurceramsoc.2023.04.061.

[22] C. Sgarlata, M.C. Ariza-Tarazona, E. Paradisi, C. Siligardi, I. Lancellotti, Use of foundry sands in the production of ceramic and geopolymers for sustainable construction materials, Appl. Sci. 13 (2023) 5166, https://doi.org/10.3390/app13085166.

[23] L. Lattanzi, A. Conte, A. Sin, J.M. Garcia, C.A. Randall, P. Colombo, Cold sintering of geopolymer powders, J. Am. Ceram. Soc. 108 (2024) e20331, https://doi.org/10.1111/jace.20331.

[24] H. Peng, T. Qi, J. Vogrin, Q. Huang, W. Wu, J. Vaughan, The effect of leaching temperature on kaolinite and meta-kaolin dissolution and zeolite re-precipitation, Miner. Eng. 170 (2021) 107071, https://doi.org/10.1016/j.mineng.2021.107071.

[25] A. Börger, P. Supancic, R. Danzer, The ball on three balls test for strength testing of brittle discs: stress distribution in the disc, J. Eur. Ceram. Soc. 22 (2002) 1425–1436, https://doi.org/10.1016/S0955-2219(01)00458-7.

[26] D. Yan, S. Chen, Q. Zeng, S. Xu, H. Li, Correlating the elastic properties of metakaolin-based geopolymer with its composition, Mater. Des. 95 (2016) 306–318, https://doi.org/10.1016/j.matdes.2016.01.107.

[27] H. Takeda, S. Hashimoto, H. Matsui, S. Honda, Y. Iwamoto, Rapid fabrication of highly dense geopolymers using a warm press method and their ability to absorb neutron irradiation, Constr. Build. Mater. 50 (2014) 82–86, https://doi.org/10.1016/j.conbuildmat.2013.09.014.

[28] V. Živica, S. Balkovic, M. Drabik, Properties of metakaolin geopolymer hardened paste prepared by high-pressure compaction, Constr. Build. Mater. 25 (2011) 2206–2213, https://doi.org/10.1016/j.conbuildmat.2010.11.004.

[29] M.W. Mervosh, S. Momjian, J. Mena-Garcia, C.A. Randall, Using percolation to design ZnO composites with hBN modified grain boundaries to obtain varistor-like behavior, Open Ceramics 20 (2024) 100707, https://doi.org/10.1016/j.oceram.2024.100707.

[30] J. Mena-Garcia, A. Ndayishimiye, Z. Fan, S.E. Perini, W. Li, B. Poudel, S. Priya, B. Foley, J. Gaskins, C.A. Randall, Sodium molybdate-hexagonal boron nitride composites enabled by cold sintering for microwave dielectric substrates, J. Am. Ceram. Soc. (2023) jace.19254, https://doi.org/10.1111/jace.19254.

[31] J. Mena-Garcia, S. Momjian, Z. Fan, A. Ndayishimiye, W. Auker, J. Gray, C. A. Randall, Multiple creep mechanisms driving densification of composites undergoing cold sintering, J. Eur. Ceram. Soc. 45 (2025) 117440, https://doi.org/10.1016/j.jeurceramsoc.2025.117440.

[32] D.J. Green, O. Guillon, J. Rödel, Constrained sintering: a delicate balance of scales, J. Eur. Ceram. Soc. 28 (2008) 1451–1466, https://doi.org/10.1016/j.jeurceramsoc.2007.12.012.

[33] F.F. Lange, Constrained network model for predicting densification behavior of composite powders, J. Mater. Res. 2 (1987) 59–65, https://doi.org/10.1557/JMR.1987.0059.

[34] J.A. DeChiara, S. Momjian, K. Wang, C.A. Randall, Bimodal grain sized barium titanate dielectrics enabled under the cold sintering process, Open Ceram. 19 (2024) 100626, https://doi.org/10.1016/j.oceram.2024.100626.

[35] A. Jabr, N. Kuzmić, S.D. Škapin, H. Jantunen, M. Nelo, M. Spreitzer, R. Bermejo, Towards high strength SrTiO₃-based composites fabricated at room temperature, J. Eur. Ceram. Soc. 44 (2024) 116782, https://doi.org/10.1016/j.jeurceramsoc.2024.116782.

[36] J. Davidovits, Geopolymers: inorganic polymeric new materials, J. Therm. Anal. 37 (1991) 1633–1656, https://doi.org/10.1007/BF01912193.

[37] P. Romero, N. Garg, Evolution of kaolinite morphology upon exfoliation and dissolution: evidence for nanoscale layer thinning in metakaolin, Appl. Clay Sci. 222 (2022) 106486, https://doi.org/10.1016/j.clay.2022.106486.

[38] G. Gadikota, F. Zhang, A. Allen, In situ angstrom-to-micrometer characterization of the structural and microstructural changes in kaolinite on heating using ultrasmall-angle, small-angle, and wide-angle X-ray scattering (USAXS/SAXS/WAXS), Ind. Eng. Chem. Res. 56 (2017) 11791–11801, https://doi.org/10.1021/acs.iecr.7b02810.

[39] P. Zemenová, A. Kloužková, M. Kohoutková, R. Král, Investigation of the first and second dehydroxylation of kaolinite, J. Therm. Anal. Calorim. 116 (2014) 633–639, https://doi.org/10.1007/s10973-014-3748-9.

[40] J. Felsche, S. Luger, Phases and thermal decomposition characteristics of hydro-sodalites Na₆₊ₓ[AlSiO₄]₆,(OH)ₓ·nH₂O, Thermochim. Acta 118 (1987) 35–55, https://doi.org/10.1016/0040-6031(87)80069-2.

[41] J.A. Pask, A.P. Tomsia, Formation of mullite from sol-gel mixtures and kaolinite, J. Am. Ceram. Soc. 74 (1991) 2367–2373, https://doi.org/10.1111/j.1151-2916.1991.tb06770.x.

[42] L. Andrini, M.R. Gauna, M.S. Conconi, G. Suarez, F.G. Requejo, E.F. Aglietti, N. M. Rendtorff, Extended and local structural description of a kaolinitic clay, its fired ceramics and intermediates: an XRD and XANES analysis, Appl. Clay Sci. 124–125 (2016) 39–45, https://doi.org/10.1016/j.clay.2016.01.049.